

pubs.acs.org/cm Article

Ion-Exchange Effects in One-Dimensional Lepidocrocite TiO₂: A Cryogenic Scanning Transmission Electron Microscopy and Density Functional Theory Study

Francisco Lagunas,*, David Bugallo, Fatemeh Karimi, Yingjie Yang, Hussein O. Badr, Jacob H. Cope, Emilio Ferral, Michel W. Barsoum, Yong-Jie Hu, and Robert F. Klie*



Cite This: Chem. Mater. 2024, 36, 2743-2755



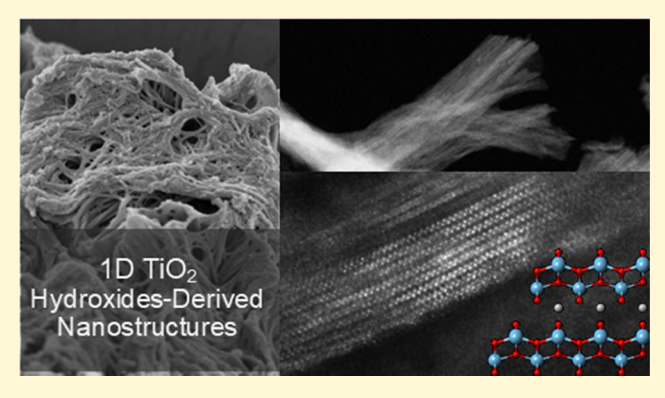
ACCESS I

III Metrics & More

Article Recommendations

s Supporting Information

ABSTRACT: One-dimensional lepidocrocite, 1DL, titania, ${\rm TiO}_2$, is a recently discovered form of this ubiquitous oxide that is of interest in a variety of applications ranging from photocatalysis to water purification, among others. The fundamental building blocks of these materials are snippets (30 nm long) of individual 1DLs that self-assemble into nanobundle, NB, structures. These NBs can then be driven to self-assemble into quasi-two-dimensional, 2D, sheets, films, or free-flowing mesoscopic particles. Here, we use analytical atomic-resolution scanning transmission electron microscopy (STEM) and first-principles density functional theory (DFT) calculations to demonstrate that the arrangement of the neighboring NFs can be altered through ion exchange with Li, Na, and tetramethylammonium hydroxide (TMA) cations. Moreover, using



cryogenic electron energy-loss spectroscopy (EELS), we show that the introduction of different ion species results in a change in the local occupancy of the TiO_2 t_{2g} and e_g orbitals. Both experimental findings are predicted by ground-state energy simulations of two-dimensional lepidocrocite TiO_2 .

■ INTRODUCTION

Titanium (di)oxides, TiO2, are ceramics of interest because a combination of their stability and chemical properties renders them promising candidates for applications ranging from pigments¹ and dyes to photocatalysts²⁻⁴ and solar cells^{5,6} among many others. Since many of these applications involve interactions at the interface of the material and its surrounding environments, the surface structure of TiO2 is an important parameter for improving its efficiency. As early as 1991, nanostructured TiO2 was synthesized—first in the form of nanotubes and later fiber-like materials—and was quickly proposed for a variety of technologies. Today, synthesizing novel TiO2 nanostructures and tuning their properties continue to be an active research field.8 With the same goal of improving the efficiency of TiO2 compounds, twodimensional (2D) counterparts of three-dimensional, 3D, TiO₂ nanomaterials are now being explored. The reduced dimensionality of 2D materials inherently offers higher specific surfaces and opens the door to the exploration of a new range of physical phenomena. 9-11

In 2021, Badr et al. reported on the synthesis of micrometersized titania flakes composed of titania-based nanofilaments (NFs), using inexpensive, earth-abundant materials in a highly scalable process. ¹² The authors reported good performance as an electrode for lithium-ion and lithium-sulfur batteries and an ability to reduce the viability of cancer cells. 12,48 At 4.1 eV, the band-gap energy, $E_{\rm g}$, of the resulting flakes is one of the highest, if not the highest value ever reported for titania-based nanostructures as a result of quantum confinement. 13 Despite the $E_{\rm g}$, the flakes' electronic band structure possessed visible light absorbance that was attributed to mid-band-gap energy states. 13 In water splitting, the flakes remained photocatalytically active (apparent quantum yield >11%) and structurally stable in water/methanol mixture for 6 months, \sim 2 weeks under irradiation of 2 suns. 14 While this material's potential for applications was clear, the exact structure of the material remained uncertain.

In 2023, we used a combination of Raman spectroscopy and direct observations of the crystal structure using an atomic-resolution scanning transmission electron microscope (STEM) to image the 2D flakes and showed them to be, in fact, composed of one-dimensional (1D) lepidocrocite TiO₂ NFs

Received: October 30, 2023 Revised: February 12, 2024 Accepted: February 14, 2024 Published: March 5, 2024





with minimal cross sections hypothesized to be in the $5 \times 7 \text{ Å}^2$ range. In addition to the weblike structures and quasi-2D films originally reported, we also observed that the TiO_2 NFs that were 20–30 nm long readily self-assembled parallel to their growth, or the [200] direction, to form larger NFs/ribbons/bundles/filaments. Peak shifts in XRD patterns between NFs washed in ethanol compared to those washed in LiCl were ascribed to the intercalation of ions between neighboring NFs.

More recently, Badr et al. presented a large-scale synthesis protocol to fully convert batches as large as 100 g of TiB₂ powders into 1D lepidocrocite NFs. 16 When dried straight from ethanol, the NFs self-assemble into nonagglomerating, free-flowing mesoporous particles (MPPs) that were \sim 13 μ m in size. Immersing the MPPs in water resulted in the disassembly of the NFs forming a highly stable colloidal suspension (zeta potential = -53 ± 9.5 mV), with concentrations of up to 40 g/L. Treating the MPPs, instead, under ambient conditions, in 10 different aqueous solutions including acids, chlorides, and sulfates of alkali, alkaline, and transition-metal salts allowed the cationic exchange of TMA+ molecules with H_3O^+ , Li^+ , Na^+ , Mg^{2+} , Mn^{2+} , Fe^{2+} , Co^{2+} , Ni^{2+} , or Zn^{2+} ions in the interfilamentous gallery. ¹⁶ Moreover, when the MPPs were exposed to U-contaminated radioactive wastewater, they showed significantly high adsorption capacity (up to 424 mg/g) coupled with a near-record selectivity coefficient (>50%) and fast adsorption kinetics. The applications of the TiB2-derived MPPs span further to polymer nanocomposites, where repairable, multifunctional, elastomeric MPPs/thiol-yne networks with NF loadings in the range of 10-60 wt.% were synthesized. 18

Here, we report on an atomic-resolution study that unambiguously determines the structure of bundles composed of 1D lepidocrocite NFs using a combination of STEM images, electron energy-loss spectroscopy (EELS) measurements conducted at room and cryogenic (96 K) temperatures, and density functional theory (DFT) calculations.

METHODS

Material Synthesis and Processing. The MPPs were prepared following our previous reports. 12,15,16 In brief, the reaction system comprises a mixture of 100 g of TiB_2 commercial powders (Thermo Scientific, - 325 mesh, PA) and 900 mL of an aqueous solution of tetramethylammonium hydroxide (TMAH, Alfa Aesar, 25 wt % in DI water, 99.9999%) split equally in five polyethylene jars. The Ti:TMA mole ratio was set to 0.6. The jars were shaken at 80 °C for 5 days, d, using a temperature-controlled incubator/shaker (211DS 49L Shaking Incubator, Labnet International Inc., NC).

The resulting reaction products/slurries were all collected in a 1 L vessel and allowed to settle down before the supernatant was disposed of. The sediment "slurry" was rinsed multiple cycles with ethanol (200 proof, Decon Lab Inc., PA). In each cycle, the sediments were stirred with ~500 mL of ethanol for 2 h using an overhead stirrer, the powders were allowed to settle, and the supernatant was again decanted and disposed of. When the pH was \approx 7, the powders were allowed to dry at 50 °C in open air for 24 h. The resulting powder was comprised of near-spherical MPPs of \approx 13 μ m in diameter, comprised, in turn, of 1DL NFs intercalated with TMA cations.

To prepare NFs intercalated with Li⁺ cations, the powders were immersed, while still wet with ethanol, in a 5 M LiCl aqueous solution and then rinsed with DI water to remove any excess LiCl salt. This step was repeated 3 times to ensure a full exchange of the TMA⁺ cations with Li. To intercalate the NFs with Na⁺ ions instead, the powders were treated similarly with a 5 M NaCl aqueous solution. All

powders were then allowed to dry at 50 °C in open air for 24 h before

The three powders will henceforth be termed TiO_2 -TMA, TiO_2 -Li, and TiO_2 -Na to refer to the NF intercalated with TMA, Li, and Na, respectively.

TEM Sample Preparation. To prepare TEM samples, a mixture of dried powders, with either pure $\rm H_2O$ or methanol, were sonicated for 15 min and then 5 mL of this mixture was drop-cast onto a 3 mm lacey carbon copper, Cu, support grid. To minimize the degree of carbon contamination, gold, Au, grids, without carbon support, were used in films that were cooled to liquid nitrogen, $\rm N_2$, temperatures. To reduce the presence of latent water, the prepared grids were placed under a heat lamp at low power and heated to $\rm 100~^{\circ}C$ for 1 h in the microscope column prior to cooling. In situ cooling STEM was conducted using a Gatan 636 liquid $\rm N_2$ double tilt cooling stage.

Focused Ion Beam, FIB, Scanning Electron Microscope, SEM, and Lamella Preparation. A cross-sectional lamella of a TiO_2 —Li mesoscopic particle was prepared using a ThermoFisher Helios 5CX FIB/SEM. The MPPs, themselves composed of 1DL nanobundles, were imaged in a SEM, and representative particles were chosen. To reduce the effects of Ga beam-related damage and to improve the structural integrity of the samples, a layer of carbon followed by tungsten was deposited on top of the region of interest. The volume surrounding the area of interest was milled away, and the lamella was lifted out with a micromanipulator. The lamella was then mounted on a Cu lift-out grid and thinned using low voltages (≤ 8 kV) and low currents (< 50 pA) to electron transparency.

STEM Imaging and Spectroscopy Conditions. STEM imaging was conducted using an aberration-corrected, cold field-emission JEOL ARM200CF operated at a 200 kV primary electron energy with the emission current at 15 μ A. The electron probe semiconvergence angle was set to 17.8 mrad at 200 kV, and the inner and outer detector angles for annular bright-field (ABF), low-angle annular dark-field (LAADF), and high-angle annular dark-field (HAADF) imagings were 11 mrad -23, 30, -120, and 68 mrad -280 mrad, respectively. The beam current for imaging was 19 nA. Images were acquired using 1024×1024 pixels with a typical pixel time of 30 μ s.

To conduct nanoscale elemental identification and quantification, we used an Oxford XMAX100TLE X-ray windowless silicon drift detector (SDD) with a 100 mm² detector area attached to the ARM200CF. 19 EELS measurements were performed using a postcolumn Gatan Continuum GIF ER spectrometer. Core-loss EELS measurements were conducted with an electron probe semiconvergence angle of 17.8 mrad and a collection angle of 53.4 mrad. Low-loss EELS and band-gap measurements were conducted at an accelerating voltage of 80 kV. The full width at half-maximum (fwhm) of the zero-loss peak was approximately 500 meV, and the sample thickness, in terms of the relative inelastic free path, was measured to be less than 0.25. The EELS and energy-dispersive spectroscopy (EDS) measurements were conducted using a beam current of 62 pA. To reduce beam-related damage, EELS maps are collected with short exposure times (<20 ms) and then 20×20 pixel regions are integrated. All core-loss spectra were aligned using the zero-loss peak (ZLP), which was simultaneously acquired using dual EELS. The tail of the ZLP was background-subtracted from core-loss spectra using a power law model, and effects from plural scattering were removed using a Fourier-ratio function.

Image Simulations. Prismatic, a program that utilizes a planewave reciprocal-space interpolated scattering matrix, was used to simulate STEM LAADF images from the DFT-generated structures. The convergence angle was set to 25 mrads, and the collection range of collection angles was 30–100 mrad. The specimen thickness was set to 2 nm.

DFT Calculations. First-principles calculations were performed based on DFT using the projector-augmented wave method (PAW)^{21,22} as implemented in the Vienna Ab initio Simulation Package (VASP).^{21,23–26} The VASPKIT code is used to assist with pre- and postprocessing.²⁷ Unless specified otherwise, the generalized gradient approximation (GGA) functional developed by Perdew–Burke–Ernzerhof (PBE) is chosen to describe the exchange–

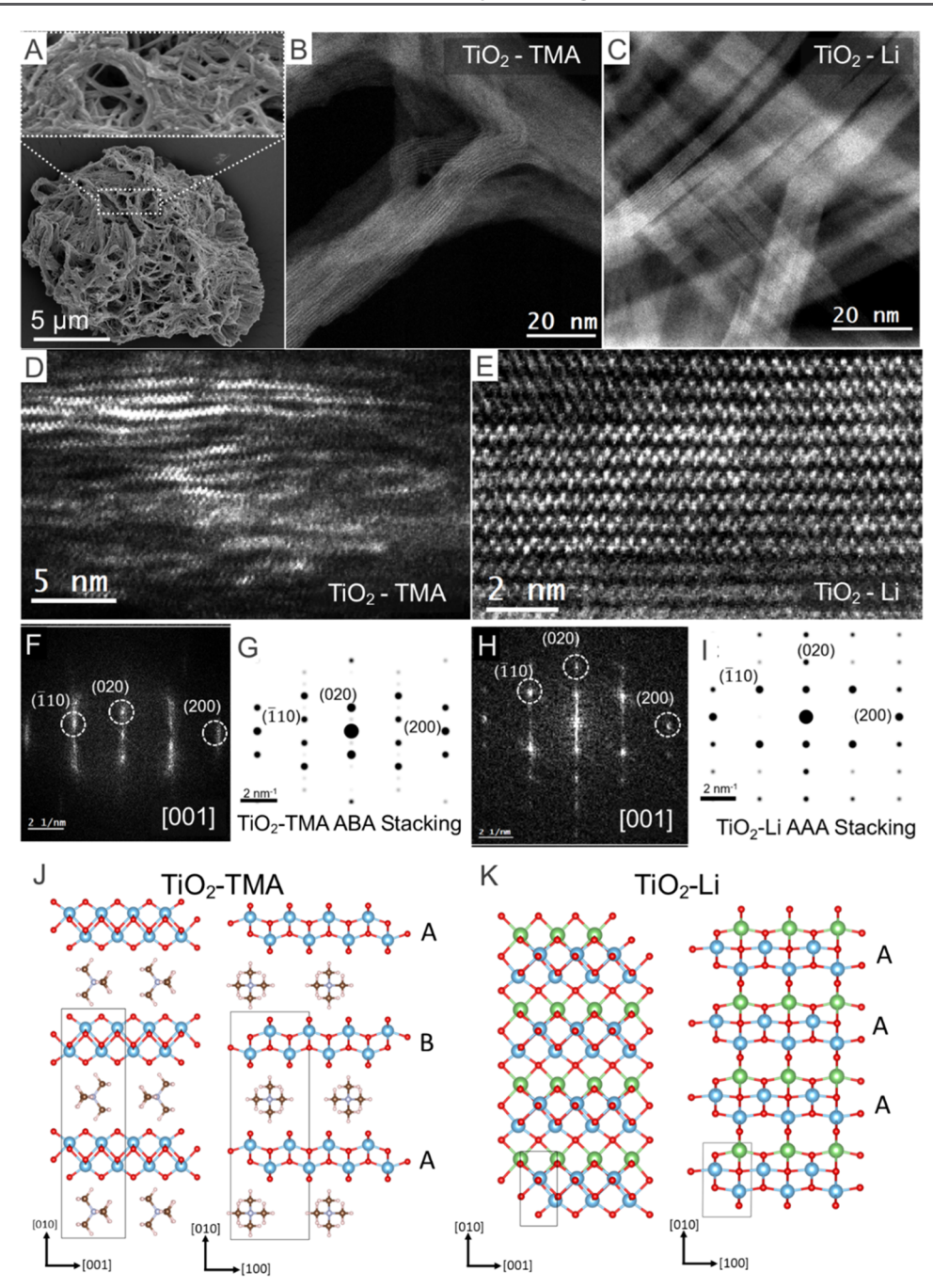


Figure 1. SEM, TEM, and DFT characterizations of 1DL NFs. (A) SEM image of a mesoscopic particle composed of 1DL NFs. Inset shows a magnified view of interwoven bundles. (B, C) HAADF images of a collection of TiO₂—TMA and TiO₂—Li bundles, respectively. Atomic-resolution images of the bundle ordering are observed in the LAADF images (D) for TMA⁺ and (E) Li⁺-exchanged samples. (F) FFT produced from the TiO₂—TMA bundle showing (200), (020), and (011) spots. (H) FFT produced from TiO₂—Li shows the (200) and (010) diffraction spots from which the center-to-center spacing can be measured. (G) SAPD generated from a structure with ABA stacking without any intercalant to simulate the b spacing observed in TEM. (I) Simulated SAPD of the (K) relaxed DFT structure of TiO₂—Li. (J) Relaxed DFT atomic structure of TiO₂—TMA. In all schematics the Ti atoms are blue, the O atoms are red the Li are green; the multipronged molecules are TMA cations

correlation interactions. ²⁸ The van der Waals interactions are accounted for using the approach by Grimme. ²⁹ The energy convergence criterion of the electronic self-consistency is set as 10^{-7} eV for the relaxation and electronic structure calculations, while the ionic relaxation is set to stop when the Hellmann–Feynman force on each atom is smaller than 0.001 eV/Å. The Brillouin-zone integration of the electronic structure is performed using a tetrahedron method with Blöchl corrections, while Gaussian-smearing is used for structure relaxation. The width of the smearing is chosen as 0.1 eV. The energy cutoff on the wave function is taken as 600 eV. A 9

 \times 9 \times 9 k-point Γ -centered mesh is used for the structural relaxations, except for the bigger unit cells (in which the base lepidocrocite, L, unit cell is repeated 3 times in any direction), for which 5 \times 5 \times 5 meshes are used. K-point meshes with densities of \sim 1000 points/Å $^{-3}$ are used. The O K-edge EELS spectra are obtained using the supercell core—hole calculations as implemented in VASP using a broadening of 0.001 eV and introducing broadening in postprocessing. It is important to note that the DFT calculations are carried out on 2D sheets of lepidocrocite, while experimentally we have NFs with a 1D

character. Despite this difference, there is good agreement between experimental and DFT calculations.

RESULTS AND DISCUSSION

Structural Changes to 1D TiO₂ from Ion Exchange. As noted in the Introduction section, once the 1DL NF snippets are formed, they self-assembled into mesoscopic particles, weblike films, or filtered quasi-2D films depending on the solvent used. ^{16,30} In this section, we describe the fundamental building blocks of these materials using atomic-resolution STEM imaging. Our findings are supported by first-principles DFT simulations of the material's lowest-energy states.

Our analysis begins with a characterization of the atomicscale ordering observed in lepidocrocite NF bundles extracted from powders containing mesoscopic particles (Figure 1A). Conglomerations of these nanobundles, NBs, were extracted by suspending dried MPPs in methanol and casting a few drops of the resulting mixture onto a TEM grid. The morphologies of the NBs varied within individual samples significantly, but in general, the NBs containing NFs exchanged with TiO₂-TMA appear more flexible and disordered than their TiO₂-Li counterparts. Typical TiO₂-TMA and TiO₂-Li NBs are shown in Figure 1B,C, respectively. In general, the former bend into one another and appear much less ordered than the latter, which appear to be more rigid, with highly ordered regions. High-resolution LAADF STEM images show that the effects of ion exchange related to local ordering can be observed at the atomic scale. Figure 1D shows a STEM image of TiO2-TMA NB with a collection of NFs with clearly observable atomic columns; neighboring regions appear to contain NFs; however, the high degree of stacking disorder makes resolving atomic columns in STEM imaging difficult. In comparison, atomic-resolution images of a TiO2-Li bundle (Figure 1E) show highly ordered stacks of NF in an NB, where the zigzag structure of the Ti backbone is clearly resolved.

The resulting DFT-relaxed structures for TiO2-TMA and TiO₂-Li layers are shown in Figure 1J,K, respectively. Comparing the structures, two key differences are observed. The first regards differences in the magnitude of the spacing between neighboring layers in the [010] direction; to accommodate the larger TMA+ molecule, the spacings between NFs increase to 10.84 Å compared to that of 6.45 Å in the Li⁺exchanged TiO2. The spacing between adjacent layers in an intermediate ion species, TiO2-Na, was calculated to be 7.56 Å (Figure S3B). Second, the relaxed DFT structures show differences in the stacking geometries of the 2D layers along the [010] direction. Adjacent TiO₂-TMA layers along the [010] direction are offset by a half-unit cell shift in the [100] direction. The resulting stacking is thus of the ABA type. The relaxed structure of the layered TiO2-Li, on the other hand, does not predict this shift, and adjacent NFs along the [010] are identical, which results in AAA stacking. These stacking differences are reflected in differences in the symmetry of the generated selected area diffraction patterns, SADPs, along the [001]. In the ABA case, odd-numbered (0k0) spots and evennumbered (0k1) diffraction spots are eliminated (Figure 1G). Crucially, these spots are present in the SADP generated from the TiO₂-Li AAA stacking (Figure 1I).

Using high-resolution S/TEM, we confirmed the atomic-scale ordering differences predicted by DFT. Using fast Fourier transforms (FFTs) generated from regions containing collections of stacked NFs, we acquired representative structural information for each sample. Figure 1H shows an

FFT with an NB of a TiO₂-Li NF consistent with the electron beam oriented along the [001] direction. The pattern is composed of [100] and [010] diffraction spots with spacings of 3.8 \pm 0.1 Å and 6.5 \pm 0.1 Å, respectively. These values contrast with the previous literature on 2D lepidocrocite ${\rm TiO}_{2^{3}}^{31,32}$ with spacings along the [010] direction typically >9 Å between TiO₂ layers. The shorter spacing here is caused by the inclusion of the Li⁺ ion and the shift to AAA stacking, resulting in a smaller lattice parameter. Nonetheless, the value is in good agreement with the value of the b-lattice parameter calculated from the DFT of 6.45 Å. Overlaying DFT-generated structures (Figure S1A) and the experimental images generated for the Li case (Figure S1B) are in excellent agreement. It is crucial to note that the latter is the distance predicted from DFT without water intercalation. The role of water in these 1D TiO₂ structures is discussed below.

The equivalent FFT spectrum for a typical TiO_2 –TMA NB is shown in Figure 1F. The LAADF image of the same sample shows that ordering along the [010] direction (Figure 1D) is reduced, and the NFs appear to be wavey, which, in turn, is reflected in the diffuse diffraction spots (Figure 1F). Even so, the differences arising from the two stacking geometries (AAA vs ABA) are clearly observed in the FFTs, such as the fact that the ABA stacking shows an absence of odd-numbered (0k0) diffraction spots. The preferential ABA geometry in TiO_2 –TMA is further supported by good agreement between experimental atomic-resolution STEM images and simulated images of NFs with ABA stacking (Figure S1C,D).

The larger degree of disorder for the TiO_2 –TMA sample resulted in a large variation of the center-to-center spacings. The average was 7.9 \pm 0.7 Å, with spacings as large as 8.9 and as small as 7.1 Å observed. This is larger than the spacing calculated for TiO_2 –Li but significantly smaller than the 10.84 Å calculated from the DFT TiO_2 –TMA structure. A likely explanation for the smaller spacings in TiO_2 –TMA is that the electron dose rates required for high-resolution imaging (500–1,000 e/Ųs) results in the decomposition of the intercalated TMA $^+$ ions. Similar results have been reported by Zhou et al. in MXenes with imido surface groups, where electron beam damage of the organic moieties results in a reduced observed basal plane spacing in STEM between neighboring Ti_3C_2 sheets as compared to XRD. 33

To acquire structural information about the TiO2-TMA NBs at low electron dosage, we utilized conventional TEM to acquire SADPs. To minimize the electron beam exposure, we prepared FIB lamellae from a region of NBs collectively aligned along a general direction, which could easily be identified using low-magnification imaging (~60 e/A2s) (Figure S2J). Two cross sections were prepared, one perpendicular and one parallel to the fiber direction. SADPs acquired at dose rates near 5-10 e/Å² showed that the two cross sections were along the [100] and [001] directions, respectively (Figure S2B,D). The symmetries of the acquired patterns are consistent with SADPs generated from the two TiO₂ DFT structures (Figure S2F,H). The values of the primary lattice parameters measured from the SADP are compared to those from the DFT structures in Figure S2I. In general, they show good agreement; the [200] and [002] values agree within the range of error, and notably, the *b*-lattice parameter measured at 21 ± 1 Å is in much closer agreement to the 21.69 Å expected from DFT.

The LAADF STEM images of the TiO₂-Na sample can be found in Figure S3. Like TiO₂-Li, the DFT TiO₂-Na

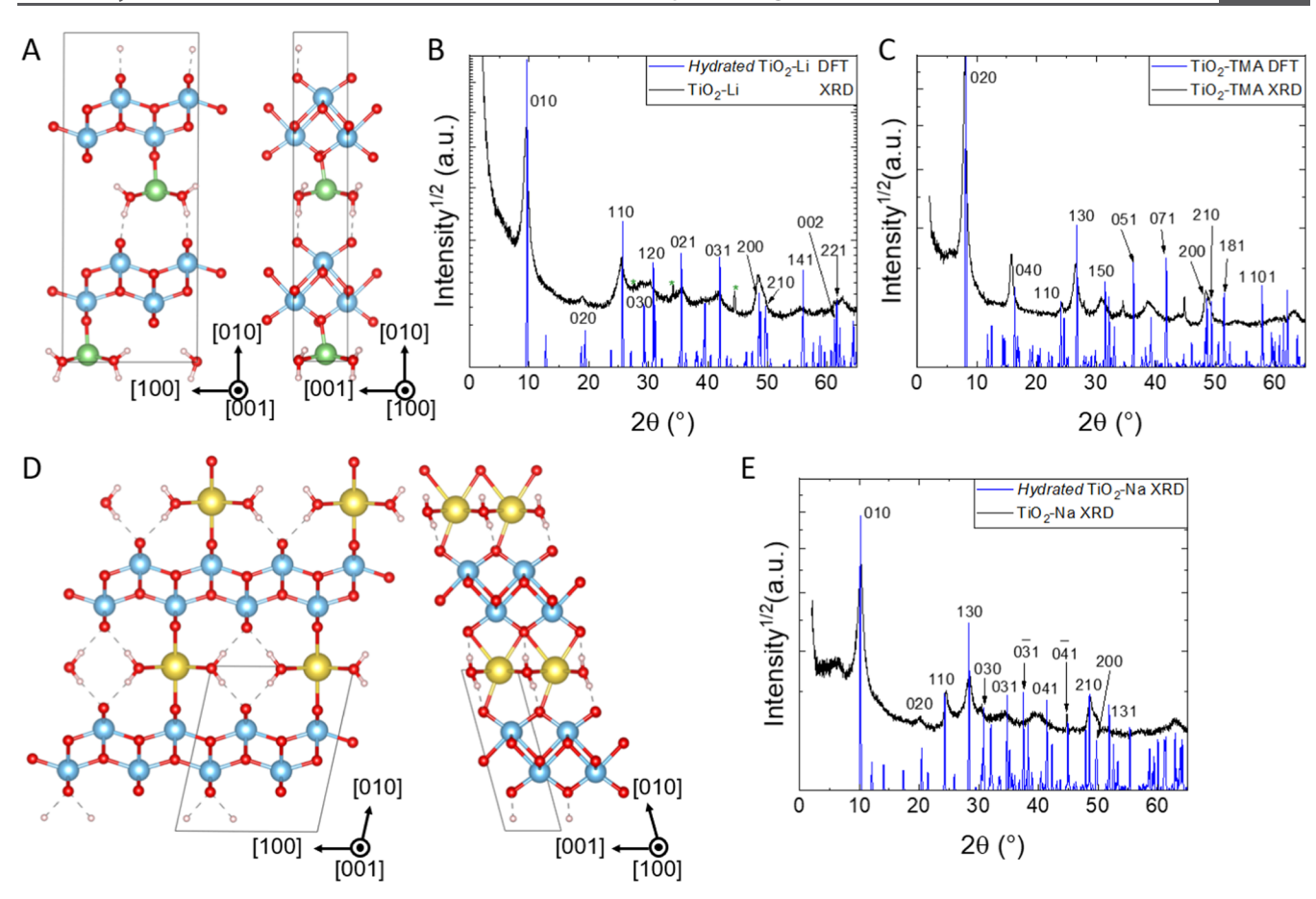


Figure 2. (A) DFT structure of water-containing TiO_2 –Li. (B) Comparison of experimental XRD patterns with peaks generated from the DFT structure. (C) Same as in panel (B) but for the TiO_2 –TMA structure shown in Figure 1J. (D) DFT structure of water-containing TiO_2 –Na. (E) Comparison of experimental XRD with the generated peaks from the DFT structure. The indexing is related to one unit cell of pure lepidocrocite, with AAA stacking in the case of panel (B) and ABA stacking for panels (C) and (E). Note in panel (E), the 0hk reflections with 1 negative and positive are separated due to the angle α not being 90° in DFT calculations. Indexing for structure (D) is available in Supplementary Table S1. Adapted with permission from [17]. Copyright 2023 Matter.

structure is predicted to exhibit AAA stacking when viewed along the [001] direction (Figure S3B). A direct comparison of simulated and experimentally acquired images seems to confirm this; however, clearer evidence of the AAA stacking in ${\rm TiO_2-Na}$ is the shared symmetries between simulated SADPs and FFTs (Figure S3E,F) generated from large regions in Figure S3A. The FFT shows that the b-lattice parameter measured in STEM is consistent with their DFT counterparts (7.3 \pm 0.1 and 7.56 Å, respectively).

While there appears to be strong agreement between the DFT structures of TiO2-Li, Na, and high-resolution STEM, the two samples present b-lattice parameters significantly smaller than those measured from XRD¹⁵. We hypothesize that this mismatch lies in the differences in the water content between the XRD and TEM samples since DFT shows that the inclusion of water in Li⁺- and Na⁺-intercalated samples modifies the structure significantly, particularly the interlayer spacing. For example, including 2 water molecules per Li⁺ ion in the TiO₂-Li structure (Figure 2A) causes the b-lattice parameter to increase to 9.87 Å, in close agreement to the 9.5 Å reported by Badr et al., 15 and giving an XRD diffraction pattern that is in remarkable agreement with the experimental one (Figure 2B). In the case of TiO2-Na, not only does the spacing increase to 9.10 Å, the stacking of the lepidocrocite layers also changes from AAA in the anhydrous case to ABA with the inclusion of water, as seen in the structure of Figure 2D. Whether we can experimentally observe this stacking change is discussed below; here, we note that the hydrated ${\rm TiO_2-Na}$ structure matches experimentally acquired XRD (Figure 2E). The diffraction patterns generated from the relaxed DFT structures also show most of the peaks with Miller indices, hkl, where $l\neq 0$ presents a higher relative intensity compared to the experimental one. This is more clearly visible in the TMA⁺-intercalated structure (Figure 2C) and implies that there is little long-range order along the c-direction, indirectly proving that the samples are mainly 1D filaments, stacked along b and grow along a.

The fact that the inclusion of water can drastically alter the low-angle spacings has been reported previously; for example, similar effects have been observed in vanadium pentoxide fibers where basal spacings decrease from 11.55 to 8.75 Šupon the evaporation of interlayer water. The fact that our STEM results more closely agree with the anhydrous structures is unsurprising when considering that the radiolysis of water occurs at dosages greater than 10 e/Ų and STEM characterization occurs in high-vacuum conditions (10^{-6} Pa partial pressure). To attempt to preserve the interlayer water, we cooled the TiO2–Li and -Na samples *in situ* to below 100 K. From there, we acquired S/TEM images and SADPs while minimizing the electron dosage incurred on the sample

(typically around 1×10^2 e/Ų). In the TiO₂–Li case, the low-dose CryoSTEM showed a spacing of 7.3 \pm 0.2 Å along the *b*-direction (Figure S4), larger than the high-dose, room-temperature STEM (6.6 \pm 0.2 Å) but well short of the DFT and XRD values (9.87 and 9.5 Å, respectively). At cryogenic temperatures, a TiO₂–Na sample also showed an increase, albeit modest, in the *b*-lattice parameter (7.6 \pm 0.1 Å at 100 K vs 7.3 \pm 0.1 Å at 293 K) but well short of the ~9 Å spacing predicted by DFT and measured by XRD. Interestingly, Figure S5 evidences that the symmetry of the SADP along the [001] has changed to ABABA, which seems to support the stacking change predicted by DFT.

Even at cryogenic temperatures, the electron dosage required to get SADPs is still well above the threshold for water. In fact, the reduced *b*-lattice parameters suggest that much of the water has been lost/damaged in the high-vacuum environment of the microscope column. It is likely that a full cryogenic STEM sample preparation—including vitrification and cold transfer into the column, using a dedicated cryo-TEM instrument—can offer valuable insights toward understanding the stability of water at low temperatures in these confined 1D materials. This, however, is beyond the scope of the work presented here and will be the focus of future work. These results are summarized in Table 1.

Table 1. Measured (b) Lattice Parameters Obtained from S/TEM and DFT Calculations as a Function of Intercalated Ion Type^a

intercalated ion	<i>b</i> -lattice parameter (S/TEM)	<i>b</i> -lattice parameter (DFT)	stacking sequence	b-LP from XRD
TMA^{+}	$21 \pm 1.0 \text{ Å (TEM low dose)}$	21.69 Å	ABABA	23.0 Å
	15.8 ± 1.4 Å (STEM high dose)			
Na ⁺	$7.3 \pm 0.1 \text{ Å}$ (STEM)	7.56 Å (anhydrous)	AAA	18.0 Å
	$15.2 \pm 0.2 \text{ Å}$ (S/TEM 96 K)	18.20 Å (hydrated)	ABABA	
Li ⁺	$6.6 \pm 0.2 \text{ Å}$ (STEM)	6.45 Å (anhydrous)	AAA	9.5 Å
	$7.3 \pm 0.2 \text{ Å}$ (S/TEM 96 K)	9.87 Å (hydrated)	AAA	

"Note that the *b*-lattice parameter for NFs exchanged with TMA⁺ and hydrated Na⁺ is doubled due to the ABAB stacking. The *b*-LP from XRD, shown in the last column, is from ref 16. Unless indicated otherwise, the S/TEM values were collected at room temperature (293 K).

Perplexingly, in several hundreds of micrographs, we did not find any conclusive atomic-resolution STEM images of the NBs acquired along the [010] direction in which ordering along the [001] direction would be *readily* observed. If the NFs were roughly square in cross section, this would be expected since the likelihood of finding NFs oriented along the [010] and [001] directions in randomly arranged NBs would be similar. By preparing an FIB thin lamella of a TiO_2 -TMA NBs—as opposed to the filtered film discussed earlier—viewed along the [100] direction (Figure 3A), we captured the atomic ordering of the NFs along their growth direction for the first time. Figure 3B shows a collection of NFs for which the Ti columns can be resolved in the LAADF STEM images. While the zigzag structure is reminiscent of the NFs viewed along the

[001] direction (Figure 1D), the spacing between neighboring Ti atoms confirms that this is the ${\rm TiO_2}$ backbone viewed along the [100] direction (Figure S6). Measuring the domain size of the NFs along the c-direction from STEM images gives an average width of 3.0 ± 1.0 nm. A histogram containing the distribution of NF widths (n=140) is shown in Figure 3D. Intriguingly, interspersed between the atomic columns are darker regions that look like nanovoids/channels. And while more work is needed to establish this, not too far-fetched observation, the presence of such channels could prove to be of great value in any application where long narrow channels are important, such as in desalination or chemical catalysis, for example.

The original aim of these experiments was to image the cross sections of the NBs. The results shown in Figure 3 afford an important glimpse of that cross section, confirming that some of the NFs do indeed stitch themselves into "wider" sheets, with an average width in the 3 nm range (Figure 3D) and with a structure that is consistent with our DFT calculations. However, this insight begs the important question of why, if individual NFs are 0.5×3 nm², the broad 3 nm side is *not* the prevalent view in the vast majority of our STEM micrographs. Said otherwise, if our NFs are linguine—and not spaghettishaped—why do we not see the broader side much more often when considering that the wider surface should by far be the more prevalent one. In individual NFs, or very dilute suspension, the fact that we do not see our presumed 5×7 $Å^2$ cross section could be related to the difficulty of imaging such thin structures using LAADF STEM images, where the image intensity scales with the atomic number, Z, and the thicknesses of the structures. Unless present in high densities, finding a 5 or 7 Å thick structure in the presence of 3-5 nm thick filaments is challenging.

In larger bundles, we have been limited to SADPs for structural information along the [010] direction (Figure S7). Notably, even these show additional reflections (marked in yellow in Figure S7C,F) indicative that there are collections of NBs in multiple orientations present even in what appears to be well-ordered bundles. Moreover, it is important to remember that when collecting atomic-resolution images, the spacing between NFs has already shrunk significantly due to the radiolysis/evaporation of water, a process that is likely to introduce a significant degree of disorder along the [010] direction.

In our previous work, we suggested that the NFs were stacked in the c-direction that we could not see because the b-lattice parameters obtained from XRD were significantly larger than those measured in the STEM. Figure 3B does not support that idea. The fact that the b-lattice parameter spacings measured from low-dose TEM micrographs of TiO_2 —TMA samples (first row in Table 1) are in decent agreement with the spacing from the low-angle peak in XRD (23.0 Å) confirms that the stacking is indeed along b, which is why the low-angle peaks are now indexed as 0k0 (Figure 2C). The differences in the b-lattice parameter between STEM images and XRD (6.6 Å vs 9.5 Å) in TiO_2 —Li case are, again, most probably due to water loss during the high electron dosage used in acquiring atomic-resolution STEM images.

To summarize this section: the NFs grow in the a-direction and stack along the b-direction. There is some growth along the c-direction. In full agreement with the titanate literature, $^{31,35-37}$ stacking in the presence of Li in anhydrous TiO₂ is AAAA, while in the presence of TMA⁺, it is ABABA.

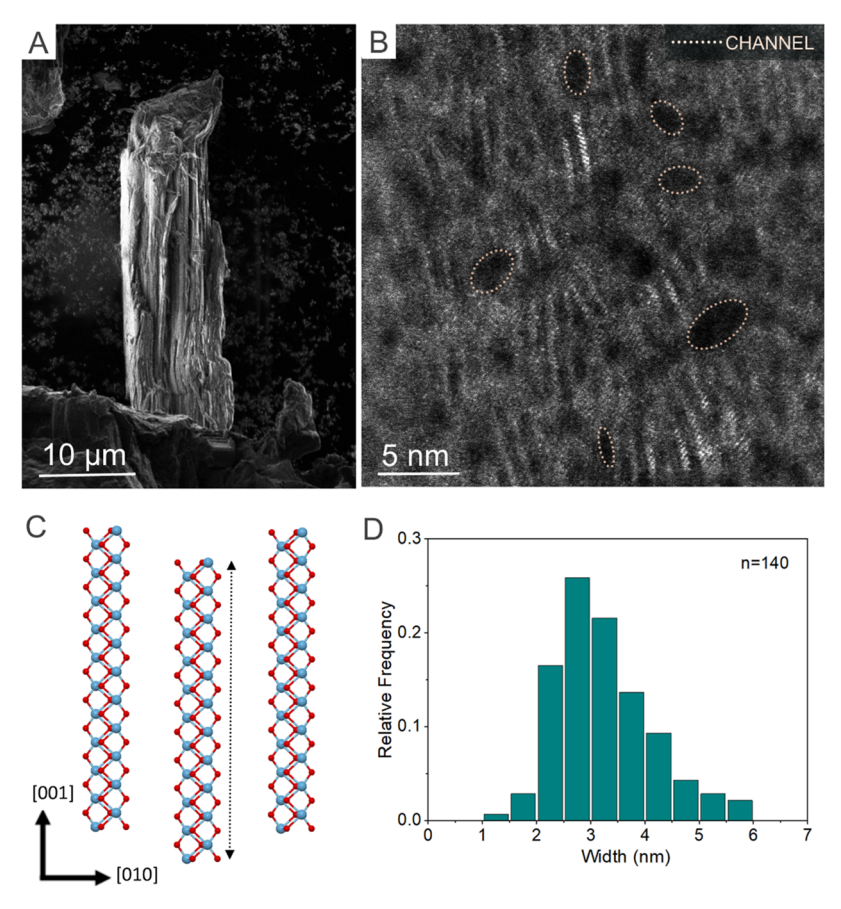


Figure 3. Characterization of cross section normal to the growth direction of TiO₂–TMA NFs, (A) SEM image of TiO₂–TMA NB. (B) LAADF STEM image along the [100] growth direction. Channels are highlighted by dashed ovals. (C) Atomic model showing TiO₂–TMA along the [100] direction. (D) Histogram showing distribution of NF widths along [001]. Lamella prepared using a dual beam FIB-SEM.

Electronic Changes Driven by Ion Exchange in 1DL

TiO₂. To probe the effects of ion interaction on the local electron bonding environment within the NBs, we acquired room-temperature, RT, as well as cryogenic EELS measurements. We began by acquiring valence EELS measurements on individual NBs from each sample. Figure 4A,B shows the low energy-loss regime for TiO2-Li and TiO2-TMA samples, respectively, from which $E_{\rm g}$ can be determined after background subtraction of the tail of zero-loss peak (Figure S8).^{38,39} It should be noted that, unlike Tauc plots, these measurements were collected on single particles or even single NBs. The band-gap energies, E_g 's, of the NFs were measured to be 3.93 \pm 0.05, 3.87 \pm 0.06, and 3.80 \pm 0.03 eV for the TMA⁺, Na⁺, and Li⁺ samples, respectively. There is roughly a 130 meV difference between TiO₂-TMA and TiO₂-Li, samples, which we suspect result from slight variations in the particle thicknesses and amounts of surface hydrocarbons present. Nonetheless, the calculated E_g 's are close to the values reported by Badr et al., 12,15 which as noted above are among the highest reported for TiO2-based compounds. 1D quantum-confinement effects are believed to be responsible for this large Eg. Importantly, the fact that we observe similar energies here implies that the NFs preserve their 1D character even when some regions appear to be ordered NBs, at least at the TEM scale.

Badr et al. characterized 1DL samples with core-loss EELS¹² and concluded that the Ti/O ratio was 1:1, inconsistent with the expected 1:2 ratio for TiO₂ or even greater values for titanates. Furthermore, the C K-edge of the reported RT

spectra exhibited a single π peak followed by a broad σ peak, commonly observed in amorphous C K-edge spectra. The source of this C—whether it is contamination, leftover suspension fluid, or TMA-remained an open question that we address here. To do so, we collected EELS at cryogenic conditions, which has been reported to significantly reduce the effects of electron beams on sensitive compounds. 40-43 Furthermore, at cryogenic temperatures, the mobility of contaminant surface hydrocarbons is reduced significantly, preventing C buildup during prolonged electron beam exposures. In TiO₂-Li samples suspended in methanol, the C concentration drops from 16 to 8 at % simply by cooling the sample to liquid N₂ temperatures. Suspending the same sample in pure H₂O further reduced the C concentration to 4 at. % (Figure S9). These results show that the solution used to suspend the powders can affect the C concentrations throughout the sample, even when the samples were allowed to dry and the measurements were conducted under highvacuum conditions (roughly 10⁻⁶ Pa pressure). The remaining observed carbon in the sample is likely trapped reactant/ washing solutions that at low temperatures possibly recondensed onto the NB surfaces.

Figure 4C compares the carbon K-edge acquired at RT (293 K) and that acquired at near-liquid N_2 temperatures (96 K). The overall shapes of the peaks are similar; however, the spectra at 96 K clearly show four well-defined peaks, labeled π_1 , π_2 , σ_1 and a. Since the C K-edge measures transitions induced by the electron beam from the occupied C 1s orbitals to the unoccupied C 2-pd-hybridized orbitals, the EELS fine structure

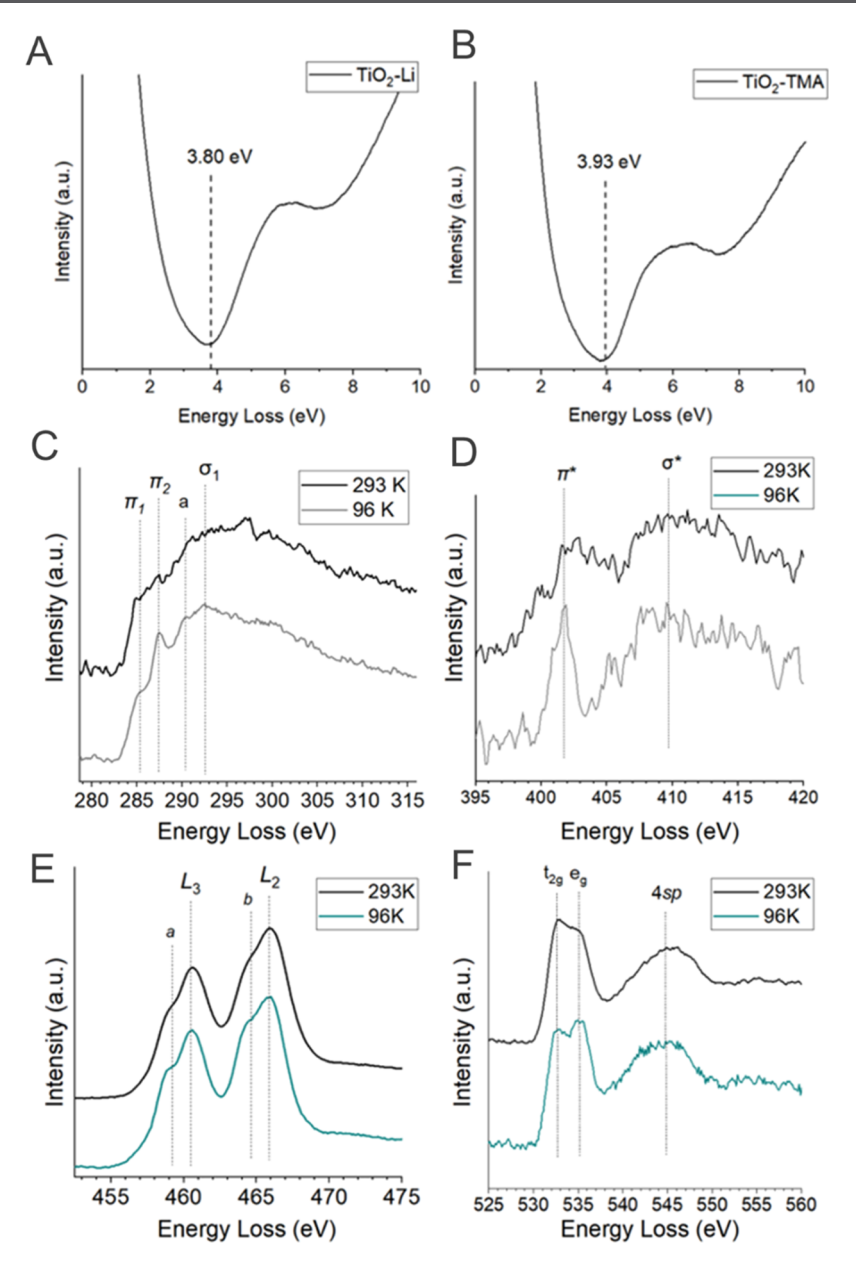


Figure 4. Room-temperature valence EELS spectra for (A) Li⁺- and (B) TMA⁺-treated NFs, collected at 80 kV. Band-gap energy, E_g , values are indicated by vertical dashed lines. A comparison of the core-loss K-edges of (C) carbon, (D) nitrogen, and (F) oxygen as well as the, (E) Ti L-edge at room vs. cryogenic temperatures for TiO₂—TMA NFs is shown. Spectra are vertically offset, and significant peaks are labeled with dashed vertical lines.

is typically sensitive to local changes in the atomic coordination surrounding the C atoms. The lack of well-defined transitions at RT is interpreted to be a result of beam-induced damage effectively breaking many C bonds. The clear presence of these peaks in the spectra collected at 96 K suggests that the beam-induced damage is sufficiently suppressed at cryogenic temperatures.

The positions of the π_1 , π_2 , a, and σ_1 peaks are 285.2, 287.5, 290.3, and 292.5 eV, respectively. The π_1 peak is also observed in spectra collected over the amorphous carbon support and can confidently be assigned to asymmetric (π) C=C bonding. In spectra collected from TiO₂-TMA NBs, the signal likely stems from decomposed TMA molecules, leftover ethanol, or other trace contaminants. Since small shifts in energy are common between different spectrometers, this peak can be used to calibrate the energy-loss position when comparing

these results to those found in the literature. Kikuma and Tonner report that the peaks corresponding to C=C π^* and C-H* peaks (from methyl-groups) are separated by 2.3 eV in polystyrene and poly[α -methylstyrene] (P α MS),⁴⁴ consistent with the 2.3 eV shift of the peak-labeled π_2 . In the same work, the authors ascribe the 5.2 eV feature above the C=C peak energy, as arising from the ionization threshold, which offers a possible explanation for the peak labeled a, which is 5.1 eV from the C=C π^* peak. The final peak (7.3 eV shift) is comparable in energy to C-C σ^* bonding observed in P α MS (7.4 eV shift); however, in the same work, they report that Ncontaining polymers, such as Nylon-6 and Nylon-66, have C-C σ^* and C-N σ^* bonds at the same energy (albeit at a higher energy value 8.4 eV from C=C π^*), which increases the possibility that the peak-labeled σ_1 corresponds to C-N bonding.

While these peak assignments are highly suggestive of the types of C bonding present in a TMA molecule (C–N, C–H), the plethora of transitions possible in a material containing C, O, and Ti combined with the fact that they are all dependent on the bonding configuration (sp², sp³, etc.) makes it difficult to definitively assign the peaks to certain transitions solely based on the C K-edge. In fact, quantitative spectroscopic studies of C-containing compounds typically use a range of energies (1–2 eV) to describe certain transitions arising from aromatic, ketones, aliphatic, and other C compounds.

The N K-edge signal, Figure 4D, is measurable only in samples containing TMA⁺. A comparison of the N K-edge at room and cryogenic temperatures shows trends similar to those observed in the C K-edge. In general, the cryogenic EELS shows narrower and more well-defined π - and σ -peaks, indicating that the effects of electron beam-induced damage are again reduced significantly at 96 K. A comparison of the N K-edge from a TMA molecule would be insightful; however, to the best of our knowledge, none have been reported in the literature.

In transition-metal oxides, the L-edge measures transitions from the 2pd-hybridized orbitals to the unoccupied 3d orbital. Here, the spectra of the Ti L-edges (Figure 4E) are composed of four peaks, the Ti L_3 - and L_2 -edges with each peak containing a shoulder at lower energies (labeled a and b in Figure 4E). The presence of the L_3 - and L_2 -peaks arises from the spin—orbit splitting of the 2pd state, and the shoulders stem from the crystal-field splitting characteristic of Ti⁴⁺ in TiO₆ octahedra. Changes in the intensities of the t_{2g} and e_g orbitals are observed in the Ti L-edge between the RT and cryogenic temperatures. They are, however, more prominent in the O K-edges shown in Figure 4F.

While the initial transition state is responsible for the crystal-field splitting in the Ti L-edge, transitions to the 2pd-hybridized, orbitals from the O 1s orbital give rise to the crystal-field splitting in the O K-edge. Since EELS measures transitions to unoccupied states, changes in the t_{2g} and e_g peak intensities relay differences in electron occupancy in each state.

The presence of well-defined transitions, observed in the C and N K-edges at 96 K, suggests that we are preserving the sensitive C bonding present in the TMA⁺ molecule. This molecule is likely responsible for the large spacing observed between stacked TiO₂—TMA NFs, and the local variation in its presence can account for the high degree of observed disorder. Interestingly, the preservation of the TMA molecule actively changes the local electronic bonding environment of the NFs themselves. This is most clearly observed in the comparison of the O K-edges collected at RT and 96 K, where the ratio of the intensity of the t_{2g} and e_g peaks is observed to change significantly.

The largest differences between core-loss spectra collected at 293 and 96 K were observed in the TMA⁺-exchanged samples. The TiO₂—Na samples exhibited clear, but less pronounced, changes in their Ti L-edge and O K-edge (Figure S10). The spectra collected from the TiO₂—Li samples appeared to be essentially identical (Figure S10). A quantitative analysis of the O K-edge shows that the degree of variation in the e_g -to- t_{2g} peak intensity ratios is greatest in the TiO₂—TMA NBs at 1.06 at 96 K vs. 0.92 at 293 K and smallest in the TiO₂—Li NFs (0.89 at 96 K vs 0.90 at 293 K). The variation observed in the TiO₂—Na sample falls within these two with an e_g -to- t_{2g} ratio of 0.94 at 96 K and 0.90 at 293 K (Table 2). These results suggest that electron beam-induced damage is most prevalent in the

Table 2. Summary of e_g -to- t_{2g} Peak Intensity Ratios as a Function of the Intercalated Ion Type^a

intercalated ion	e_g/t_{2g} (96 K)	e_g/t_{2g} (293 K)	e_g/t_{2g} (DFT)
TMA^{+}	1.06	0.92	1.50
Li ⁺	0.89	0.90	0.76
Na ⁺	0.94	0.90	

^aThese values are extracted from O K-edge spectra acquired at 96 K and RT. Ratios of the peak intensities of the e_g -to- t_{2g} predicted from DFT are listed in the last column and are in qualitative agreement with those measured from EELS at 96 K (column 2).

 TiO_2 —TMA samples and plays a lesser role in changing the bonding environments for the TiO_2 —Na and -Li NFs. This is mirrored by the fact that the TiO_2 —Li samples are observed to be significantly more stable to STEM imaging than their TiO_2 —TMA counterparts.

More importantly, from an electronic point of view, our DFT calculations correctly predict the fact that the e_g/t_{2g} ratios for TiO $_2$ -Li and TiO $_2$ -TMA samples are, respectively, < 1.0 and >1.0. This is important since it lends important credibility to our DFT calculations. This agreement is somewhat surprising, however, given that in the experiment our NFs are closer to 1D than the 2D lepidocrocite sheets we modeled. Similarly, DFT predictions (Figures 1J,K and 2A), using the 2D structure, while maybe not exact, give results quite close to the experiment. We are currently developing 1DL DFT models.

By comparing the core-loss spectra of ${\rm TiO_2-TMA}$, -Na, and -Li NFs at cryogenic conditions, we can quantify the effects of ion exchange on the local ${\rm TiO_2-bonding}$ environment, while minimizing the effects of electron beam-induced damage. In Figure 5A,B, we compare the Ti L- and the O K-edges, respectively, of all three samples where we, again, observe variations in the e_g and t_{2g} 's orbital intensities. In general, we find that the larger the size of the exchanged ion, the larger the e_g -to- t_{2g} ratio. Whether these differences arise from differences in the density of the ions on the surface or the increased center-to-center spacing is explored in the next section.

The DFT-calculated electronic density of states (DOS) for pristine, Li⁺-intercalated, and TMA⁺-intercalated 2D lepidocrocite TiO2 show consistent results with the experimental observation. As shown in Figure 5C, a slightly smaller band gap for the TiO₂-Li is observed in comparison with the TMA⁺intercalated lepidocrocite (2.92 eV for Li⁺, 2.96 eV for pure TiO₂, and 3.18 eV for TMA⁺), in accordance with the observed trend in EELS. There is a clear underestimation of the values compared to the measured ones, which is expected when using the conventional PBE functionals;⁴⁷ however, the trend is well represented. More importantly, the difference in the projected DOS values of the 3d t_{2g} and e_g orbitals of the Ti atoms explains the change in the EELS spectra with intercalated cation species. According to the projected eDOSs of the Ti 3d orbitals (Figure 5D), the ratio between the number of unoccupied t_{2g} and e_g states $(A_{t_{2g}}/A_{e_g})$ is calculated and shown in Figure 5E. There is a higher amount of unoccupied t_{2g} states in the Li⁺-intercalated structure than in the TMA+ case, and both have more than the pure structure. Furthermore, since the actual concentration of TMA⁺ is probably much lower than that in the DFT calculations, we would expect that a mixture of the pure and TMA+-calculated A_{t_0}/A_{e_0} ratios to be closer to the real ones observed in EELS.

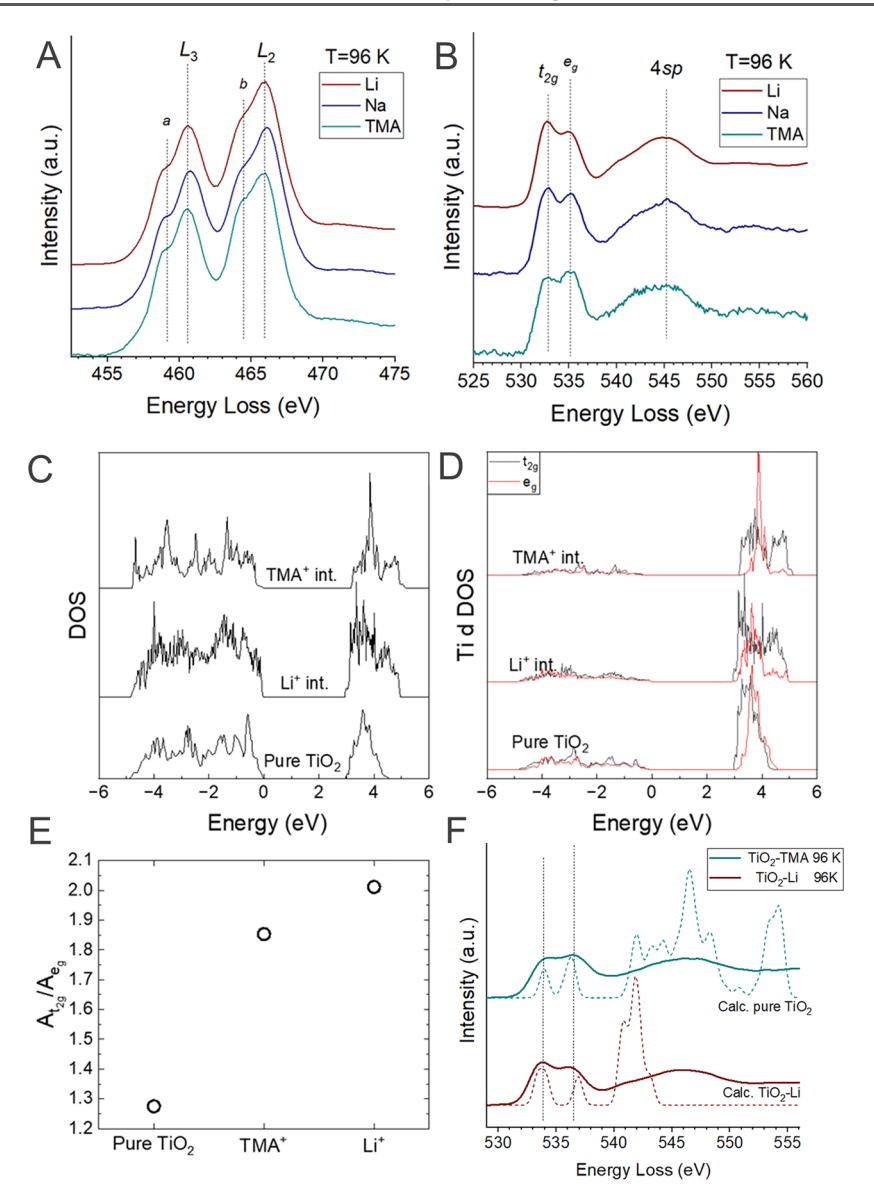


Figure 5. Characterization of the electronic structure of NFs as a function of intercalation. (A) Comparison of the Ti L-edge and (B) the O K-edge for Li⁺-, Na⁺-, and TMA⁺-treated NFs collected at cryogenic temperatures (96 K). Calculated electronic density of states, DOS, for the pure lepidocrocite structured TiO₂-, Li⁺-, and TMA⁺-intercalated structures. (C) Total and (D) DOS of Ti d orbitals. (E) DFT-derived ratio of areas of the DOS of Ti t_{2g} and e_g orbitals for the three different structures in the conduction band. (F) O K-edge for Li⁺- and TMA⁺-treated NFs compared with the ones obtained from DFT for Li⁺-intercalated and pure TiO₂ structures. Calculated spectra are shifted along the x-axis to fit the position of the first peak as DFT cannot reproduce the exact energy of the transitions. Solid lines are experimental results; dotted lines are calculated ones.

We also performed supercell core—hole calculations to obtain the theoretical EELS spectra of the pure and the Li⁺-intercalated lepidocrocite. The results (Figure 5F) show a clear change in the relative intensities of the t_{2g} and e_g peaks from the pure structure to the Li⁺-intercalated case. We expect that the TMA⁺-intercalated TiO₂ would lead to a similar spectrum as the pure one, as, discussed above, there are NF regions that appear to be TMA⁺ free. Therefore, the change in the electronic structure of the NFs is clearly explained by the effect of the intercalating species, with Li⁺ causing a shift in the relative intensities of the O K-edge t_{2g} and e_g peaks.

CONCLUSIONS

Using a variety of HRTEM, SEM/FIB, and EELS techniques on self-assembled ${\rm TiO_2}$ -based NBs, we show that the nature of the ion—Li⁺, Na⁺, or TMA⁺ cations—between the NFs affects

both the physical and electronic properties of these NBs. Given that the NFs tend to self-order parallel to their [100] growth direction, the NB morphologies are inherently tied to the bonding strengths between them. Our analysis identified three key insights into the arrangement of NFs in the NBs. First, we show, in agreement with the titanate literature and our DFT calculations of ground-state structures, that when Li+ is in between the 1D lepidocrocite NFs, the stacking along b is AAA and ABA in the TMA and Na cases. Second, while it is likely that the fundamental unit of the NFs is approximately square in cross section, our analysis reveals that a number of NFs combine along the c-direction, forming ribbon-like structures with an average width of around 3 nm. Longitudinal channels may also be present parallel to the NFs growth direction. Finally, using cryogenic STEM, we showed differences in the occupancies of the t_{2g} and e_g orbitals between TiO₂-Li and

 ${
m TiO_2}$ -TMA materials. These differences are confirmed by the electronic DOS calculations from DFT that show a different density of e_g and t_{2g} orbitals in the conduction band with the intercalation of ${
m Li}^+$ in the structure.

At \approx 3.9 eV, the $E_{\rm g}$ values obtained from EELS are in good agreement with those measured from Tauc plots of bulk films and colloid suspensions. This agreement is gratifying and consistent with our notion that the higher $E_{\rm g}$ values measured are due to quantum confinement.

The fact that the fundamental properties of these 1D $\rm TiO_2$ -based materials can be altered by ion exchange is exciting, considering the large variety of intercalatable ions. Divalent and metallic ion species (Mg²⁺, Mn²⁺, Fe²⁺, Co²⁺, Ni²⁺, or $\rm Zn^{2+}$) can open the door to applications in chemical, electro, and photocatalysis. Combined with the fact that these $\rm TiO_2$ NFs can be manufactured into free-flowing mesoscopic powders, two-dimensional sheets or films open the door to a variety of potential applications. If nanometric channels are present in the NBs, then they could prove important in many applications where confined fluid flow is important.

ASSOCIATED CONTENT

Supporting Information

The Supporting Information is available free of charge at https://pubs.acs.org/doi/10.1021/acs.chemmater.3c02773.

Direct comparisons of simulated DFT and experimental STEM images; focus ion beam preparation of films and particles; additional TEM characterizations and EELS chemical characterizations; and comparisons of DFT structures and XRD patterns (PDF)

AUTHOR INFORMATION

Corresponding Authors

19104, United States

Francisco Lagunas — Department of Physics, University of Illinois Chicago, Chicago, Illinois 60616, United States; orcid.org/0000-0002-6377-683X; Email: flagun2@uic.edu

Robert F. Klie – Department of Physics, University of Illinois Chicago, Chicago, Illinois 60616, United States;

orcid.org/0000-0003-4773-6667; Email: rfklie@uic.edu

Authors

David Bugallo — Department of Material Science & Engineering, Drexel University, Philadelphia, Pennsylvania 19104, United States; Centro de Investigación en Química Biolóxica e Materiais Moleculares (CIQUS), Departamento de Química-Física, Universidade de Santiago de Compostela, 15782 Santiago de Compostela, Spain

Fatemeh Karimi – Department of Physics, University of Illinois Chicago, Chicago, Illinois 60616, United States

Yingjie Yang — Department of Physics, University of Illinois Chicago, Chicago, Illinois 60616, United States;
orcid.org/0000-0002-1898-8171

Hussein O. Badr – Department of Material Science & Engineering, Drexel University, Philadelphia, Pennsylvania

Jacob H. Cope – Department of Material Science & Engineering, Drexel University, Philadelphia, Pennsylvania 19104, United States

Emilio Ferral — Department of Physics, University of Illinois Chicago, Chicago, Illinois 60616, United States Michel W. Barsoum — Department of Material Science & Engineering, Drexel University, Philadelphia, Pennsylvania 19104, United States; oorcid.org/0000-0001-7800-3517

Yong-Jie Hu — Department of Material Science & Engineering, Drexel University, Philadelphia, Pennsylvania 19104, United States

Complete contact information is available at: https://pubs.acs.org/10.1021/acs.chemmater.3c02773

Author Contributions

F.L. and D.B. contributed equally.

Notes

The authors declare no competing financial interest.

ACKNOWLEDGMENTS

This project was supported by the National Science Foundation (DMR-2309396 and DMR-2211319) and made use of instruments in the Electron Microscopy Service at the UIC Research Resources Center. The acquisition of UIC JEOL JEM ARM200CF was supported by an MRI-R² grant from the National Science Foundation (Grant No. DMR-0959470), and the upgraded Gatan Continuum spectrometer was supported by a grant from the NSF (DMR-1626065). This work made use of the ThermoFisher Helios 5CX (cryo)FIB-SEM instrument in the Electron Microscopy Core of UIC's Research Resources Center, which received support from UIC, Northwestern University, and ARO (W911NF2110052). The use of instrumentation at the UIC Research Resources Center (RRC-East) is acknowledged. D.B. acknowledges the funding received from the European Union through the Marie Skłodowska-Curie Actions Postdoctoral Fellowship (ref 101063432). The DFT calculations were carried out using the Stampede2 cluster at the TACC through allocation MAT220033 from the Advanced Cyberinfrastructure Coordination Ecosystem: Services & Support (ACCESS) program, which was supported by the U.S. National Science Foundation Grants #2138259, #2138286, #2138307, #2137603, and #2138296.

■ REFERENCES

- (1) Braun, J. H.; Baidins, A.; Marganski, R. E. TiO₂ Pigment Technology: A Review. *Prog. Org. Coat.* **1992**, 20 (2), 105–138.
- (2) Fujishima, A.; Honda, K. Electrochemical Photolysis of Water at a Semiconductor Electrode. *Nature* **1972**, 238 (5358), 37–38.
- (3) Khan, S. U. M.; Al-Shahry, M.; Ingler, W. B. Efficient Photochemical Water Splitting by a Chemically Modified N-TiO₂. *Science* **2002**, 297 (5590), 2243–2245.
- (4) Linsebigler, A. L.; Lu, G.; Yates, J. T. Photocatalysis on ${\rm TiO_2}$ Surfaces: Principles, Mechanisms, and Selected Results. *Chem. Rev.* **1995**, 95 (3), 735–758.
- (5) Liu, J.; Kuo, Y.-T.; Klabunde, K. J.; Rochford, C.; Wu, J.; Li, J. Novel Dye-Sensitized Solar Cell Architecture Using TiO₂-Coated Vertically Aligned Carbon Nanofiber Arrays. *ACS Appl. Mater. Interfaces* **2009**, *1* (8), 1645–1649.
- (6) Burschka, J.; Pellet, N.; Moon, S.-J.; Humphry-Baker, R.; Gao, P.; Nazeeruddin, M. K.; Grätzel, M. Sequential Deposition as a Route to High-Performance Perovskite-Sensitized Solar Cells. *Nature* **2013**, 499 (7458), 316–319.
- (7) Bavykin, D. V.; Friedrich, J. M.; Walsh, F. C. Protonated Titanates and ${\rm TiO_2}$ Nanostructured Materials: Synthesis, Properties, and Applications. *Adv. Mater.* **2006**, *18* (21), 2807–2824.
- (8) Wang, X.; Li, Z.; Shi, J.; Yu, Y. One-Dimensional Titanium Dioxide Nanomaterials: Nanowires, Nanorods, and Nanobelts. *Chem. Rev.* 2014, 114 (19), 9346–9384.

- (9) Ma, J.; Reeves, K. G.; Porras Gutierrez, A.-G.; Body, M.; Legein, C.; Kakinuma, K.; Borkiewicz, O. J.; Chapman, K. W.; Groult, H.; Salanne, M.; Dambournet, D. Layered Lepidocrocite Type Structure Isolated by Revisiting the Sol—Gel Chemistry of Anatase TiO₂: A New Anode Material for Batteries. *Chem. Mater.* **2017**, 29 (19), 8313—8324.
- (10) Hu, Y.; Li, Y.; Cheng, J.; Chen, M.; Fu, W.; Liu, B.; Zhang, M.; Shen, Z. Intercalation of Carbon Nanosheet into Layered TiO₂ Grain for Highly Interfacial Lithium Storage. *ACS Appl. Mater. Interfaces* **2020**, *12* (19), 21709–21719.
- (11) Kim, I. Y.; Jo, Y. K.; Lee, J. M.; Wang, L.; Hwang, S.-J. Unique Advantages of Exfoliated 2D Nanosheets for Tailoring the Functionalities of Nanocomposites. *J. Phys. Chem. Lett.* **2014**, *5* (23), 4149–4161.
- (12) Badr, H. O.; El-Melegy, T.; Carey, M.; Natu, V.; Hassig, M. Q.; Johnson, C.; Qian, Q.; Li, C. Y.; Kushnir, K.; Colin-Ulloa, E.; Titova, L. V.; Martin, J. L.; Grimm, R. L.; Pai, R.; Kalra, V.; Karmakar, A.; Ruffino, A.; Masiuk, S.; Liang, K.; Naguib, M.; Wilson, O.; Magenau, A.; Montazeri, K.; Zhu, Y.; Cheng, H.; Torita, T.; Koyanagi, M.; Yanagimachi, A.; Ouisse, T.; Barbier, M.; Wilhelm, F.; Rogalev, A.; Björk, J.; Persson, P. O. Å.; Rosen, J.; Hu, Y.-J.; Barsoum, M. W. Bottom-up, Scalable Synthesis of Anatase Nanofilament-Based Two-Dimensional Titanium Carbo-Oxide Flakes. *Mater. Today* **2022**, *54*, 8.
- (13) Colin-Ulloa, E.; Martin, J. L.; Hanna, R. J.; Frasch, M. H.; Ramthun, R. R.; Badr, H. O.; Uzarski, J. R.; Barsoum, M. W.; Grimm, R. L.; Titova, L. V. Electronic Structure of 1D Lepidocrocite TiO_2 as Revealed by Optical Absorption and Photoelectron Spectroscopy. *J. Phys. Chem. C* **2023**, *127* (15), 7275–7283.
- (14) Badr, H. O.; Natu, V.; Neaţu, Ş.; Neaҳu, F.; Kuncser, A.; Rostas, A. M.; Racey, M.; Barsoum, M. W.; Florea, M. Ultra-Stable, 1D TiO₂ Lepidocrocite for Photocatalytic Hydrogen Production in Water-Methanol Mixture. *Matter* **2023**, *6*, 1–17, DOI: 10.1016/j.matt.2023.05.026.
- (15) Badr, H. O.; Lagunas, F.; Autrey, D. E.; Cope, J.; Kono, T.; Torita, T.; Klie, R. F.; Hu, Y.-J.; Barsoum, M. W. On the Structure of One-Dimensional TiO₂ Lepidocrocite. *Matter* **2023**, *6*, 128.
- (16) Badr, H. O.; Cope, J.; Kono, T.; Torito, T.; Lagunas, F.; Castiel, E.; Klie, R. F.; Barsoum, M. W. Titanium Oxide-Based 1D Nanofilaments, 2D Sheets, and Mesoporous Particles: Synthesis, Characterization, and Ion Intercalation. *Matter* 2023, 6 (0), 3538–3554, DOI: 10.1016/j.matt.2023.07.022.
- (17) Wang, L.; Badr, H. O.; Yang, Y.; Cope, J. H.; Ma, E.; Ouyang, J.; Yuan, L.; Li, Z.; Liu, Z.; Barsoum, M. W.; Shi, W. Unique Hierarchical Structures of One Dimensional Lepidocrocite Titanate with Cation-Exchangeable Sites for Extraordinary Selective Actinide Capture for Water Purification. *Chem. Eng. J.* 2023, 474, No. 145635.
- (18) Wilson, O. R.; Carey, M. S.; Cope, J. H.; Badr, H. O.; Nantz, J. M.; ElMelegy, T. A.; Barsoum, M. W.; Magenau, A. J. D. Repairable Reinforced Composites of 1D TiO₂ Lepidocrocite Mesoparticles and Thiol-Yne Click Networks via Alkylborane-Initiated in Situ Polymerization. *Cell Rep. Phys. Sci.* **2023**, *4*, No. 101434.
- (19) Phillips, P. J.; Paulauskas, T.; Rowlands, N.; Nicholls, A. W.; Low, K.-B.; Bhadare, S.; Klie, R. F. A New Silicon Drift Detector for High Spatial Resolution STEM-XEDS: Performance and Applications. *Microsc. Microanal.* **2014**, 20 (4), 1046–1052.
- (20) Rangel DaCosta, L.; Brown, H. G.; Pelz, P. M.; Rakowski, A.; Barber, N.; O'Donovan, P.; McBean, P.; Jones, L.; Ciston, J.; Scott, M. C.; Ophus, C. Prismatic 2.0 Simulation Software for Scanning and High Resolution Transmission Electron Microscopy (STEM and HRTEM). *Micron* 2021, 151, No. 103141.
- (21) Kresse, G.; Joubert, D. From Ultrasoft Pseudopotentials to the Projector Augmented-Wave Method. *Phys. Rev. B* **1999**, *59* (3), 1758–1775.
- (22) Blöchl, P. E. Projector Augmented-Wave Method. *Phys. Rev. B* **1994**, *50* (24), 17953–17979.
- (23) Kresse, G.; Furthmüller, J. Efficient Iterative Schemes for Ab Initio Total-Energy Calculations Using a Plane-Wave Basis Set. *Phys. Rev. B* **1996**, *54* (16), 11169–11186.

- (24) Kresse, G.; Furthmüller, J. Efficiency of Ab-Initio Total Energy Calculations for Metals and Semiconductors Using a Plane-Wave Basis Set. *Comput. Mater. Sci.* **1996**, *6* (1), 15–50.
- (25) Kresse, G.; Hafner, J. Ab Initio Molecular-Dynamics Simulation of the Liquid-Metal–Amorphous-Semiconductor Transition in Germanium. *Phys. Rev. B* **1994**, 49 (20), 14251–14269.
- (26) Kresse, G.; Hafner, J. Ab Initio Molecular Dynamics for Liquid Metals. *Phys. Rev. B* **1993**, 47 (1), 558–561.
- (27) Wang, V.; Xu, N.; Liu, J.-C.; Tang, G.; Geng, W.-T. VASPKIT: A User-Friendly Interface Facilitating High-Throughput Computing and Analysis Using VASP Code. *Comput. Phys. Commun.* **2021**, 267, No. 108033.
- (28) Perdew, J. P.; Burke, K.; Ernzerhof, M. Generalized Gradient Approximation Made Simple. *Phys. Rev. Lett.* **1996**, 77 (18), 3865–3868
- (29) Grimme, S. Semiempirical GGA-type density functional constructed with a long-range dispersion correction. *J. Comput. Chem.* **2006**, 27 (15), 1787–1799.
- (30) Sudhakar, K.; Karmakar, A.; Badr, H. O.; El-Melegy, T.; Hassig, M. Q.; Carey, M.; Masiuk, S.; Wu, L.; Qian, Q.; Kono, T.; Li, C. Y.; Barsoum, M. W. One-Dimensional, Titania-Based Lepidocrocite Nanofilaments and Their Self-Assembly. *Matter* **2023**, *6* (9), 2834–2852.
- (31) Ma, R.; Bando, Y.; Sasaki, T. Nanotubes of Lepidocrocite Titanates. Chem. Phys. Lett. 2003, 380 (5), 577-582.
- (32) Gao, T.; Fjellvåg, H.; Norby, P. Raman Scattering Properties of a Protonic Titanate $H_x Ti_{2-x/4} \square_{x/4} O_4 \cdot H_2 O$ (\square , Vacancy; x = 0.7) with Lepidocrocite-Type Layered Structure. *J. Phys. Chem. B* **2008**, *112* (31), 9400–9405.
- (33) Zhou, C.; Wang, D.; Lagunas, F.; Atterberry, B.; Lei, M.; Hu, H.; Zhou, Z.; Filatov, A. S.; Jiang, D.; Rossini, A. J.; Klie, R. F.; Talapin, D. V. Hybrid Organic–Inorganic Two-Dimensional Metal Carbide MXenes with Amido- and Imido-Terminated Surfaces. *Nat. Chem.* **2023**, *15*, 1722–1729.
- (34) Legendre, J.-J.; Livage, J. Vanadium Pentoxide Gels:: I. Structural Study by Electron Diffraction. *J. Colloid Interface Sci.* **1983**, 94 (1), 75–83.
- (35) Makise, K.; Takei, T.; Saito, N.; Yamanaka, J.; Kumada, N.; Mori, H.; Itoi, N.; Goto, T. Crystal Structure and Ion-Exchange Property of a Lepidocrocite-like Sodium Titanate. *J. Asian Ceram. Soc.* **2023**, *11* (1), 170–177.
- (36) Sasaki, T.; Watanabe, M.; Hashizume, H.; Yamada, H.; Nakazawa, H. Macromolecule-like Aspects for a Colloidal Suspension of an Exfoliated Titanate. Pairwise Association of Nanosheets and Dynamic Reassembling Process Initiated from It. J. Am. Chem. Soc. 1996, 118 (35), 8329–8335.
- (37) Sasaki, T.; Watanabe, M.; Michiue, Y.; Komatsu, Y.; Izumi, F.; Takenouchi, S. Preparation and Acid-Base Properties of a Protonated Titanate with the Lepidocrocite-like Layer Structure. *Chem. Mater.* **1995**, 7 (5), 1001–1007.
- (38) Rafferty, B.; Brown, L. M. Direct and Indirect Transitions in the Region of the Band Gap Using Electron-Energy-Loss Spectroscopy. *Phys. Rev. B* **1998**, *58* (16), 10326–10337.
- (39) Yan, X.; Jin, Q.; Jiang, Y.; Yao, T.; Li, X.; Tao, A.; Gao, C.; Chen, C.; Ma, X.; Ye, H. Direct Determination of Band Gap of Defects in a Wide Band Gap Semiconductor. ACS Appl. Mater. Interfaces 2022, 14 (32), 36875–36881.
- (40) Zhang, P.; Han, B.; Yang, X.; Zou, Y.; Lu, X.; Liu, X.; Zhu, Y.; Wu, D.; Shen, S.; Li, L.; Zhao, Y.; Francisco, J. S.; Gu, M. Revealing the Intrinsic Atomic Structure and Chemistry of Amorphous LiO₂-Containing Products in Li-O₂ Batteries Using Cryogenic Electron Microscopy. *J. Am. Chem. Soc.* **2022**, *144* (5), 2129–2136.
- (41) Wang, X.; Li, Y.; Meng, Y. S. Cryogenic Electron Microscopy for Characterizing and Diagnosing Batteries. *Joule* **2018**, 2 (11), 2225–2234.
- (42) Zachman, M. J.; Tu, Z.; Choudhury, S.; Archer, L. A.; Kourkoutis, L. F. Cryo-STEM Mapping of Solid-Liquid Interfaces and Dendrites in Lithium-Metal Batteries. *Nature* **2018**, *560* (7718), 345–349.

- (43) Colby, R.; Williams, R. E. A.; Carpenter, D. L.; Bagués, N.; Ford, B. R.; McComb, D. W. Identifying and Imaging Polymer Functionality at High Spatial Resolution with Core-Loss EELS. *Ultramicroscopy* **2023**, 246, No. 113688.
- (44) Kikuma, J.; Tonner, B. P. XANES Spectra of a Variety of Widely Used Organic Polymers at the C K-Edge. J. Electron Spectrosc. Relat. Phenom. 1996, 82 (1), 53–60.
- (45) Lajaunie, L.; Pardanaud, C.; Martin, C.; Puech, P.; Hu, C.; Biggs, M. J.; Arenal, R. Advanced Spectroscopic Analyses on a:C-H Materials: Revisiting the EELS Characterization and Its Coupling with Multi-Wavelength Raman Spectroscopy. *Carbon* **2017**, *112*, 149–161.
- (46) Le Guillou, C.; Bernard, S.; De la Pena, F.; Le Brech, Y. XANES-Based Quantification of Carbon Functional Group Concentrations. *Anal. Chem.* **2018**, 90 (14), 8379–8386.
- (47) Wang, L.; Wei, D.; Kang, S.; Xie, X.; Shi, Y.; Liu, S. Two-Dimensional Titania: Structures and Properties Predicted by First Principle Calculation. *J. Phys. Chem. C* **2018**, 122 (40), 22911–22919.
- (48) Cardoza, N. A.; Badr, H. O.; Pereira, R.; Barsoum, M.; Kalra, V. One-Dimensional, Titania Lepidocrocite-based, Nanofilaments and Their Polysulfide Anchoring Capabilities in Lithium Sulfur Batteries. ACS Appl. Mater. Interfaces 2023, 15, 50973.